STUDENT JOURNAL OF PHYSICS

INTERNATIONAL EDITION

STUDENT JOURNAL OF PHYSICS

This is a quarterly journal published by Indian Association Of Physics Teachers. It publishes research articles contributed by Under Graduate and Post Graduate students of colleges, universities and similar teaching institutions, as principal authors.

STUDENT JOURNAL OF PHYSICS

Scope of the Journal

The journal is devoted to research carried out by students at undergraduate level. It provides a platform for the young students to explore their creativity, originality, and independence in terms of research articles which may be written in collaboration with senior scientist(s), but with a very significant contribution from the student. The articles will be judged for suitability of publication in the following two broad categories:

1. **Project based articles**
   These articles are based on research projects assigned and guided by senior scientist(s) and carried out predominantly or entirely by the student.

2. **Articles based on original ideas of student**
   These articles are originated by the student and developed by him/ her with possible help from senior advisor. Very often an undergraduate student producing original idea is unable to find a venue for its expression where it can get due attention. SJP, with its primary goal of encouraging original research at the undergraduate level provides a platform for bringing out such research works.
   It is an online journal with no cost to the author.

Since SJP is concerned with undergraduate physics education, it will occasionally also publish articles on science education written by senior physicists.

Information for Authors

- Check the accuracy of your references.
- Include the complete source information for any references cited in the abstract. (Do not cite reference numbers in the abstract.)
- Number references in text consecutively, starting with [1].

- Language: Papers should have a clear presentation written in good English. Use a spell checker.

Submission

1. Use the link "Submit" of Website to submit all files (manuscript and figures) together in the submission (either as a single .tar file or as multiple files)
2. Choose one of the Editors in the link "Submit" of Website as communicating editor while submitting your manuscript.

Preparation for Submission

Use the template available at "Submit" section of Website for preparation of the manuscript.

Re-Submission

- For re-submission, please respond to the major points of the criticism raised by the referees.
- If your paper is accepted, please check the proofs carefully.

Scope

- SJP covers all areas of applied, fundamental, and interdisciplinary physics research.

Determining Detector Threshold and Material Thickness Using an Alpha-Emitter Source

Mira Ghazali[1,3,*], Daniele Dell'Aquila[3,], Man Yee Betty Tsang[2,3,#]**

[1] 3rd Year Undergraduate, Department of Physics, Michigan State University, East Lansing, MI 48824 USA
[2] Department of Physics, Michigan State University, East Lansing, MI 48824 USA
[3] National Superconducting Cyclotron Laboratory, Michigan State University, East Lansing, MI 48824 USA

Abstract: Double-Sided Silicon Strip Detectors of the High-Resolution Array (HiRA), recently used in a heavy ion experiment at the National Superconductive Cyclotron Laboratory (Michigan State University), have been calibrated using a uranium-232 radioactive source. Parameters important for the analysis of the experiment, such as the thickness of a Sn-Pb foil used to protect the Si detectors from radiation damage and the detector electronic thresholds, have been inferred using radioactive source data.

Keywords: Silicon Strip Detectors, HiRA, Radiation damage

1. INTRODUCTION

A recent experiment was conducted at the National Superconducting Cyclotron Laboratory (NSCL) to study the Equation of State (EoS) of nuclear matter. The properties of the nuclear EoS are fundamental not only to our understanding of nuclei, but also to correctly describe complex astrophysical objects such as Neutron Stars [1]. To this end, the experiment aimed to measure the ratio of neutron to proton energy spectra emitted in the isotopes of Ca+Sn and Ca+Ni nuclear collisions at E/A=56-140 MeV, which is predicted to be sensitive to the properties of the nuclear EoS and is needed to constraint Neutron Stars observables. To detect neutrons and charged particles in a single experiment, a complex coupling of several nuclear physics detectors (as shown in Fig. 1) was implemented, including two Neutron Walls (NWs), the Veto Wall (VW), the Forward Array (FA), the Microball, and the High-Resolution Array (HiRA). While the combination of FA, VW and NWs (the latter constituted by large arrays of bars containing a liquid scintillator) allows to measure neutrons, HiRA (located at the right side of the vacuum chamber in Fig. 1), is used to detect, with high precision, charged particles and fragments [2].

This paper spotlights HiRA and the various elements of the detector. The paper focuses, in particular, on the procedure used to obtain energy calibration of the Double-Sided Silicon Strip Detectors (DSSSDs) in HiRA, the analysis of the electronic detection thresholds, and the study of the thickness of a material absorber placed at the entrance widows of the detectors during the experiment.

* ghazalim@msu.edu, ** dellaqui@nscl.msu.edu, # tsang@nscl.msu.edu
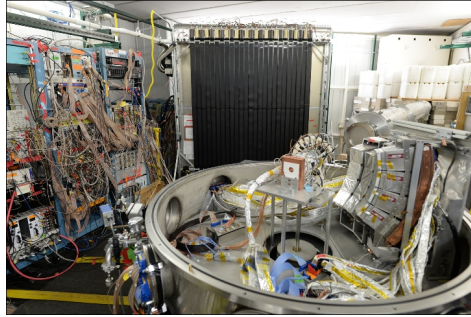
Figure 1: A photograph of the experimental setup at the National Superconducting Cyclotron Laboratory. A circular vacuum chamber (of around 50 cm radius) contains the experiment target, lying in the center of the chamber inside the Microball, and a cluster of 12 HiRA telescopes placed at the right side at a distance of around 35 cm from the target. The beam direction is from bottom left to top right of the picture. The first NW is placed at around 4 m from the target.

2. EXPERIMENTAL DETAILS

2.1 The High Resolution Array
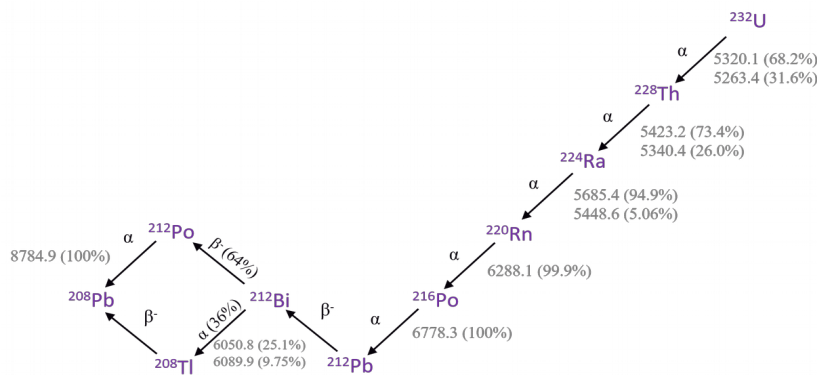
Figure 2: The decay scheme of ^{232}U. Alpha and beta decays are indicated. In the case of the alpha-decay, kinetic energies (MeV) of the emitted alphas and the corresponding emission probabilites are shown. The decay chain ends with ^{208}Pb.

HiRA is an array of highly segmented detectors for charged particles which combine detectors based on semiconducting material and scintillators [3]. HiRA provides exceptional energy resolution that is fundamental for the advancement of our exploration of the Equation of State. It is composed of modular telescopes, 12 telescopes are used in the present experiments arranged in the configuration 4x3 shown in Fig. 1, each containing two separate detection stages: a silicon detector as the first stage (around 1500 μm thick, ΔE) and four (4) Cesium-Iodide (CsI) Crystals used as the second detection stage (with a thickness of 10 cm in order to stop most particles, E). When a particle strikes a HiRA telescope, the combination of

ΔE, the energy deposited by the particle in the first detection stage, and E, the residual energy released in one of the CsI detectors, is used to identify the type of particle (via the so-called ΔE-E technique) and its kinetic energy (as the sum ΔE+E). Additionally, the impact point on the surface of the telescope, which allows to obtain the emission direction of the particle from the experiment target (where it is produced), is deduced from the segmentation in vertical and horizontal *strips* of the electrode used to collect the charge from the silicon detection stage. The latter, is a square silicon piece of dimensions 7.5 cm x 7.5 cm and a thickness of around 1500 μm. An ultra-thin aluminium layer (≈0.59 μm), used as ohmic contact to connect the silicon to a detection circuit, is deposited on front and back faces of the silicon to measure the number of electron-hole pairs produced in the silicon by the incident particle. Such number is proportional to the energy released by the particle in the material, being ≈3.62 eV, the energy required to produce one of such pairs [3]. To provide information on the impact point of the particle on the surface of the silicon, as mentioned above, the aluminium layer is segmented in 32 vertical strips on the front face and 32 horizontal strips on the back face, with a width of 2 mm, which provide 32 independent electric contacts on both sides to form 1024 detection pixels.

2.2 Energy Calibrations of DSSSDs

To individually calibrate each of the strips of HiRA DSSSDs, we used a Uranium-232 radioactive alpha-source. This source consists in a metallic disc on which the radioactive material is deposited, covered with a thin gold layer (0.093 μm). ^{232}U is a natural alpha-emitter that decays, with a life-time $T_{1/2}$=68.9 years, to ^{228}Th emitting an alpha-particle (2 protons and 2 neutrons, a nucleus of ^{4}He) of an energy around 5.3 MeV. The decay chain is made by subsequent alpha and beta decays of the daughter nucleus, ^{228}Th, terminating with ^{208}Pb as shown, schematically, in Fig. 2. Each transition between isotopes in the decay scheme of ^{232}U is identified in Fig. 3, where the alpha energy spectrum obtained from one strip of HiRA is shown as a histogram of counts. Here, the x-axis is in Analog to Digital Converter (ADC) channels, the "raw" information collected by the acquisition system. Peaks, of well-known energy, identified in this plot, allow to calibrate the strip with a linear calibration. We used four of the peaks identified in Fig. 3, and labelled in green, since they are the only peaks isolated in the detected spectrum. This procedure has been performed, individually, for each strip (front and back) of each HiRA telescope.

Once the raw data is received in ADC channels for one of the detection strips, it can be converted into MeV by using the corresponding linear calibration. A spectrum, analogous to the one shown in Fig. 3 is shown in Fig. 4 with the blue line. To increase statistics, we have combined data from all the strips of a single telescope after calibration. Peaks identified in Fig. 3, and relative to each particular alpha-transition, are well visible in the calibrated spectrum, testifying the good quality of our calibrations.
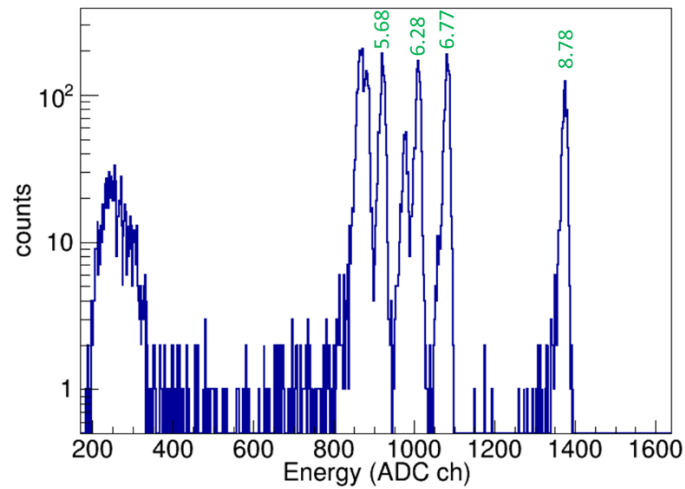
Figure 3: Alpha spectrum of a uranium-232 radioactive source detected with one strip of HiRA (telescope 0). Alpha-particles in this energy range are completely stopped in the first detection stage of HiRA. Data is reported in uncalibrated ADC channels. Peaks correspond to well-identified alpha-transitions. The peak at around 300 ch is caused by gamma-rays emitted by the source.
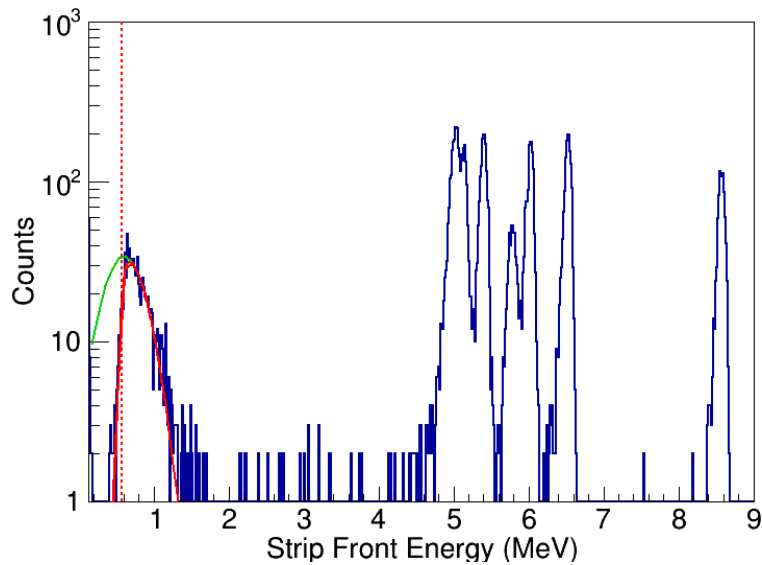
Figure 4: Fit of the gamma-peak observed with one front strip of HiRA. The fit is obtained with the combination of a Gaussian and a Fermi function (to simulate the effect of the detection threshold). The green curve shows the Gaussian function only as resulted from the fit. The red line is the global fit function. A red dashed line indicates the position of the deduced threshold. The example is produced by using data of a typical strip from telescope 0.

3. THRESHOLD ANALYSIS

The alpha-spectrum shown in Fig. 3 exhibits a peak at low ADC channels (around 300 ch), corresponding to energies lower than 1 MeV. Such peak is caused by gamma-rays emitted by the ^{232}U-source and detected by the silicon detectors. The gamma peak appears slightly distorted in its low energy tail, indicating that it lies around the detection threshold, i.e. the minimum energy that a particle must release in the silicon and overcome the electronic circuit to trigger the acquisition of the corresponding signal. This thresholds are normally difficult to pin-point with experimental data due to the low pulses coming from noise of the electronic circuits. Knowledge of the Si detector thresholds is important for the determination of the highest energy of the protons detected in the telescopes.

A study of the shape of the gamma peak can therefore provide useful evidence of the location of such threshold. By fitting it with the product of a Gaussian function $G(x) = a*exp[(x-b)^2/2c^2]$ where a, b and c are free parameters, to simulate an ideal gamma peak unaffected by threshold, and a Fermi function

$$F(x) = \frac{d}{1+\exp\left(\dfrac{x-E_{thr}}{\Delta E_{thr}}\right)},$$ where d is a free parameter and $E_{thr} \pm \Delta E_{thr}$ is the detection threshold, to

simulate the fall of the left tail due to threshold effects, one can analyze the rise of this peak to infer the threshold value strip-by-strip. An example of this fit obtained for one of the front strips of HiRA is shown in Figure 5. The red curve is the result of the fit, while the green curve corresponds to the Gaussian function, resulted from the fit, as one would observe if a threshold effect was not present. A dashed red curve indicates the obtained threshold value. Figure 6 shows the threshold in MeV by telescope for all of the front strips, obtained with the method here described. The electronic thresholds for most telescopes are around 0.5 MeV. In the case of Telescope 2, due to noise in the electronics for that telescope, the threshold is slightly higher to 0.8 MeV.
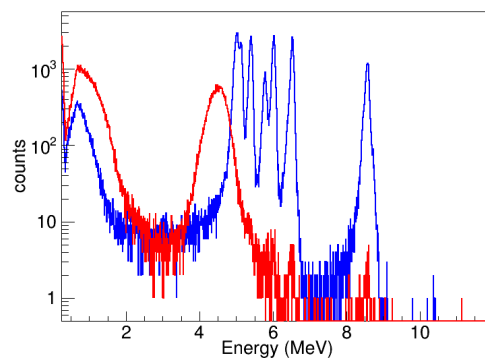
*Figure 5: Calibrated alpha-particle spectrum obtained by combining data of HiRA strips of an entire telescope (32 strips, telescope 0 in our array). The blue spectrum is obtained without the use of the Sn/Pb absorber, while the red one is obtained when the Sn/Pb absorber is placed at the entrance window of the telescope. The latter is affected by straggling effects, broadening the observed peaks.*
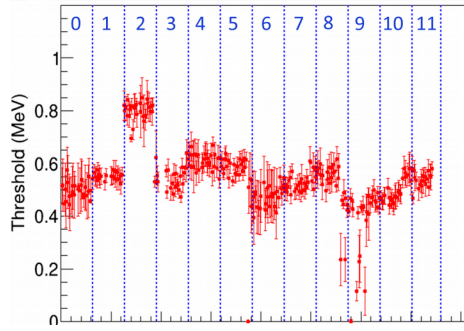
Figure 6: Threshold values in MeV for each of the strip front of HiRA. Dashed vertical blue lines indicate the limits of each of the 12 telescopes.

4. STUDY OF ABSORBER THICKNESS

Each of the 12 telescopes is covered with three (3) layers of tin-lead (Sn-Pb) foils, placed in front of the DSSSDs, to protect detectors from damage caused by the intense flux of electrons that is usually emitted in nuclear collisions involving heavy ions at these energies. Each foil has a thickness of approximately six (6) microns based on the information from the manufacturer resulting in a total of about18 micron thick foil at the entrance window of each telescope. This acts as an absorber as it completely stops electrons, but also degrades the energy particles carry prior to reach the detectors. For this reason, the energy measured by detectors is not the actual energy carried by particles as they are emitted from the target. As an example, after passing through the 18 µm absorber foil, the theoretical E_{final} of an alpha-particle emitted with an initial energy $E_{initial} = 8.78 \, MeV$, results to be around 4.9 MeV. The effect of the interaction with a material of a heavy charged particle can be universally parametrized by the Bethe formula. This relates the stopping power $\dfrac{dE}{dx}$ of an incident heavy ion, which corresponds to the energy lost by the particle per unit of length traveled in the material, to energy, charge and mass of the particles and the properties of the material:

$$-\frac{dE}{dx} = 4\pi N_e r_e^2 m_e c^2 \frac{Z^2}{\beta^2} \left(\ln \frac{2 m_e c^2 \beta^2 \gamma^2}{I} - \beta^2 - \frac{\delta(\gamma)}{2} \right) \qquad [1]$$

Here, the properties of the material are represented by I, the material ionization potential, and N_e, the electron density per unit of volume, while the properties of the incident particle are charge Z and speed β. $\delta(\gamma)$ is a relativistic correction term that depends on the Lorentz factor γ of the incident particle. The Bethe formula can be used to infer the thickness of the Sn-Pb absorber by using alpha-particles emitted by the ^{232}U source interacting with the Sn-Pb foil.

While the relative uniformity of the foil is very good, the thickness, on the other hand, has a slight error. This uncertainty has a significant impact on the reconstructed incident energy of particles passing through the material. A larger thickness corresponds to a greater energy loss, according to equation 1.

In order to perform an accurate correction of detected energy for the energy loss in the absorber, it is important to accurately determine the thickness of the absorber over each of the 12 telescopes. This can be achieved by measuring the residual energy of alpha-particle of well-known energy, after passing through the absorber. The corresponding spectrum, calibrated in MeV, is shown with the red line in Fig. 4, compared to the one obtained without the absorber (the blue line). After passing through the absorbers, only two broad peaks are visible on the spectrum. Between these two peaks there is a relatively large gap indicating that the 8.78 MeV alpha peak is isolated from possible contaminations caused by neighbour peaks. The 8.78 MeV energy peak of the [232]U source appears at an energy around 4 MeV in the absorbed spectrum in Fig. 4.

By extracting the energy position of this peak for each strip, one can obtain the value that corresponds to the energy deposited in the detector by the alpha-particle particle. This value can then be used to calculate, by means of the equation 1, the energy loss by the particle in the Sn/Pb foil, and deduce the thickness of the foil itself. This calculation has been performed by means of the software LISE++ [4]. The vast majority of the strips recorded an energy that was less than 4.9 MeV (the energy predicted for a nominal 18 microns thickness of the absorber). With this information, it is evident that the thickness of the foils are all greater than the nominal thickness provided by the manufacturer because more energy is being lost after passing through the absorber. Thickness values obtained with a strip-by-strip analysis have been averaged within each telescope of HiRA to generate the thickness mapping in Fig. 7, they range from around 18.2 µm to 21 µm. This analysis is particularly important to correct the detected energy for the absorber material that they punch-through before reaching the detectors.
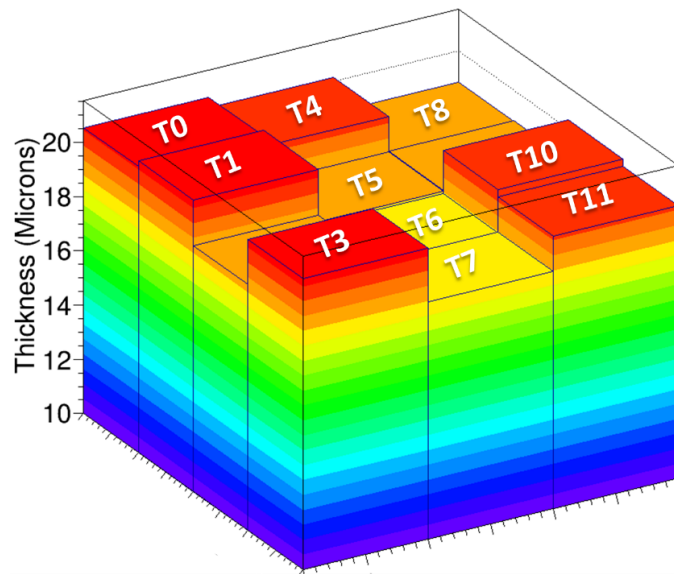

Figure 7: Thickness mapping of the Sn/Pb foils (for each telescope) obtained by means of the described analysis. Telescopes are numbered from 0 to 11 as shown by the labels.

5. CONCLUSIONS

In conclusion, energy calibration and detector characterization of HiRA DSSSDs and its electronic thresholds have been obtained by analyzing alpha emitted from a uranium-232 radioactive source. The energy calibration has been performed by means of a linear function using four well-known alpha-transitions observed in the obtained energy spectra, strip-by-strip. A precise study of detection threshold was possible using a low-energy gamma peak observed in the alpha spectrum. The product of a Gaussian function and a Fermi function was used to consistently fit the shape of this peak and infer the position in energy of the detection threshold in the electronics. Threshold values have been found to lie from 0.5 to 0.8 MeV. Finally, a study of the energy degradation of alpha-particles that punch through a Sn-Pb absorber (placed in front of the HiRA telescopes during the experiment) has been carried out to infer the thickness of the Sn-Pb absorber foil. This analysis is important since it allows measurement of the absorber thicknesses, telescope-by-telescope. We found thickness values ranging from 18.2 μm to 21 μm, instead of a nominal thickness of 18 μm for all the foils with the error given by the manufacturer. The accurate foil thicknesses allows consistently correct the energy of detected particles in HiRA.

6. ACKNOWLEDGEMENTS

References

[1] P. Danielewicz, R. Lacey, and W. G. Lynch, Science 298, 1592 (2002).

[2] M.S. Wallace et al., Nucl. Instr. Meth. A 583 (2007) 302.

[3] Glenn .F. Knoll, Radiation Detection and Measurement, John Wiley & Sons Inc., 1979, Canada.

[4] LISE++: Exotic Beam Production with Fragment Separators. URL: http://lise.nscl.msu.edu/lise.html.

Simulation and Fitting of Magnetic Fields of Superconducting Multipole Magnets at FRIB

Michael C. Wentzel[1]

[1]3rd Year Undergraduate, Department of Physics, University of Michigan, Ann Arbor, MI 48109, USA

Abstract. Essential to the beam delivery system at the Facility for Rare Isotope Beams (FRIB) is the precise calibration of steering and focusing magnets along the beam line. To properly calibrate multipole magnets used in the beam delivery system, the field throughout the bore of the magnet must be known. Specifically, when modeling or measuring multipole magnets with both large apertures and short lengths the fringing field at the edges of the field distribution must be accounted for. Moreover, the magnets in the beam line are not pure multipoles and thus exhibit behavior associated with dipole, quadrupole, sextupole, and other harmonics. Here we present an analysis of the mathematical and computational methods used to simulate and study the magnetic field within multipole magnets.

Keywords: Magnetic Field, Quadrupole, Modeling, FRIB, Curve Fitting, Enge Function.

1. INTRODUCTION

We carry out a numerical implementation of the results presented by Hiroyuki Takeda et al. [1] in the paper on the extraction of 3D field maps from 2D surface measurements. The process is acutely useful in the case of superconducting magnets due to their predilection for yoke saturation. We discuss here the specific case of short-length, large-aperture superconducting quadrupoles (SQs) which are used extensively in the beam delivery system at the Facility for Rare Isotope Beams.

An Enge function product was used to model the on-axis gradient for the superconducting quadrupoles (denoted as $b_{2,0}$) [1]. The model was then used to simulate the on-axis gradient at multiple currents, since the shape of the field varies significantly over the operating range of the quadrupole. We tested the accuracy of four similar fitting algorithms by fitting the parameters of the Enge function product to the simulated data and observing the deviation from the previously known parameters used in the simulation.

2. MODELING THE ON-AXIS GRADIENT FUNCTION

An on-axis gradient function is a mathematically convenient way of defining the magnetic field at any point inside the bore of a multipole magnet using a function of a single variable. The magnetic field inside the bore is determined by Laplace's equation of the magnetic scalar potential, $\nabla^2 \Phi = 0$, with Φ defined in cylindrical coordinates owing to the geometry of the magnets. Solving for Φ and

applying the conditions that the scalar potential be single-valued and the length of the magnet be finite, we can achieve the following expression for Φ [1].

$$\Phi(r, \theta, z) = \sum_{n=1}^{\infty} \sum_{m=0}^{\infty} \left[\frac{b_{n,m}(z)r_0}{n+2m} \left(\frac{r}{r_0} \right)^{n+2m} sin(n\theta) + \frac{a_{n,m}(z)r_0}{n+2m} \left(\frac{r}{r_0} \right)^{n+2m} cos(n\theta) \right]$$

(1)

Here n represents the multipole harmonic of the magnet (i.e. dipole, quadrupole, etc.). We can see that the functions $b_{n,m}(z)$ and $a_{n,m}(z)$ (on-axis gradient functions) can be used to describe the behavior of the normal and skew magnetic field within a multipole. In fact, it has been shown that it is sufficient to find only the $m = 0$ term from which all further terms can be determined. [1, 2] For our purposes, we are interested in the normal component of a superconducting quadrupole magnet, and thus we focus on $b_{2,0}(z)$. While an analytic solution for $b_{2,0}(z)$ does exist, we model the on-axis gradient at the centers of the SQs using the product of two fifth order Enge functions as shown in Eq. (2).

$$b_{2,0}(z) = \frac{B_0}{(1 + exp(\sum_{n=0}^{5} c_{i_n}(\frac{z - L_{eff}/2}{2r_0})^n))} \times \frac{1}{(1 + exp(\sum_{m=6}^{11} c_{e_m}(\frac{-z - L_{eff}/2}{2r_0})^m))}$$

(2)

As in the solution for the magnetic potential Φ, cylindrical coordinates were used such that multipole fields about the longitudinal axis can be used for focusing charged particle beams. The longitudinal axis, here labeled z, refers to the position along the reference beam axis relative to the center of the magnet, and r_0 is the reference radius at which the magnetic field is measured (often treated as the radius of the pole-tips). Here c_{i_n} and c_{e_m} represent the incident and exit Enge function coefficients respectively, and the constant B_0 is a factor corresponding to the maximum on-axis gradient value. The effective length of the SQ, L_{eff}, is a parameter associated with the length of the magnet which can be defined in a number of ways provided the definition is consistent for each calculation. Throughout our tests of the fitting process, we used two methods of determining effective length.

The first method of effective length determination was to simply set the length to a fixed constant. When using experimental SQ data, the analogous step simply would be to probe for an effective length at a particular current and set L_{eff} to that value for all other field and current calculations. As explained in the following section, this was the method used to simulate the data. The second method for determining SQ effective length accounted for a variable effective length as a function of current. The formula used to define effective length is shown in Eq. (3) below where $b_{2,0}$ is a measurement of the on-axis gradient. In Eq. (3) $b_{2,0}(z = 0)$ is the value of the on-axis gradient at the center of the z axis of the magnet (presumably the maximum gradient value). It is possible in experiment for the maximum value to stray slightly from the center at $z = 0$; however, we chose to

set the measurement at a fixed position. Note that in practice, the integral would turn into a discrete Riemann sum evaluated over the region of data acquisition.

$$\frac{L_{eff}}{b_{2,0}(z=0)} = \int_{-\infty}^{\infty} b_{2,0}(z)dz \tag{3}$$

To further adjust the model to account for variable current, another variation was accounted for. The Enge coefficients (c_{i_n} and c_{e_n}) vary with excitation current, I, and can usually be described by a second or higher degree polynomial relation. We chose a second order polynomial for the purpose of testing different techniques of fitting the data to the model. Therefore, each coefficient is related to current by Eq. (4).

$$c_{i_n}, c_{e_n} = p_0 + p_1 I + p_2 I^2 \tag{4}$$

Applying this relation, we simulated test data for a known set of polynomial coefficients. We then implemented various fitting approaches to fit the data to the models and determine which methods gave the smallest residual errors.

3. DATA SIMULATION

We simulated the on-axis gradient of a quadrupole to behave as the model in Eq. (2). Each Enge coefficient (c_{i_n} and c_{e_n}) was modeled as a second order polynomial in current I as in Eq. (4). The parameters p_n were chosen to mimic similar behavior observed in an SQ designed for the FRIB separator. Additionally, the parameters were set such that for each n, the behavior for the polynomials c_{i_n} and c_{e_n} matched. At ten currents spaced evenly between 18 and 180 Amps, we simulated gradients along z with z set to vary between -1 and 1 m and the step size set to $5mm$. In the simulation we used a constant effective length set to $0.7m$. The length approximately marks where the on-axis gradient drops to half its maximum value for any given current. The final simulated on-axis gradient data were therefore a function both of z position and current. Fitting methods for the solution to the polynomial coefficients could then be tested against known values.

4. FITTING METHODS

We tested four different methods to fit the polynomial coefficients, p_n, and then compared the residuals from each of the three fits. All the methods were performed using the ROOT software with the Minuit minimization package. The methods differed in the technique used to determine effective length and global or local fitting of the p_n parameters with respect to the dimension of current. Local (or indirect) fitting was performed by fitting the Enge coefficients, c_{i_n} and c_{e_n}, for each current individually and then using the results of each coefficient for all ten currents to reach the objective of fitting the polynomial coefficients, p_n, for each c_{i_n} and c_{e_n}. Global (or direct) fitting was performed by fitting the polynomial coefficients in Eq. (4) for each c_{i_n} and c_{e_n} while considering the data over all currents.

First, we performed a local, indirect fit of the polynomial coefficients while treating L_{eff} as a constant value of $0.7m$, as was simulated. Since our data were generated using that set length, the fit using a constant length was predicted to be more accurate. However, it is important to note that in an experimental setting, one would not have knowledge of this value and would use Eq. (3) to determine its value. Note that the normalization of Eq. (3) is such that one does not necessarily get the same value of L_{eff} as was used in simulating the data. This has implications on the resulting fitted coefficients as will be demonstrated below.

Using the set effective length, we individually fit each of the generated data sets for the ten currents valued at $18n$ amps with $n \in 1, ..., 10$. Each fit generated values for the Enge coefficients (c_{i_n} and c_{e_n}). These values were plotted with the y-axis corresponding to the coefficient value and the x-axis corresponding to current. Finally, each coefficient was fit to a second degree polynomial to determine each p_n.

Second, we performed a local, indirect fit using a calculated effective length according to Eq. (3). The integral was evaluated numerically over the interval $z \in [-1, 1]$. Beyond this domain, the on-axis gradient becomes negligible. This calculated effective length was then substituted into Eq. (2), and the remainder of the fitting procedure followed as in the first method.

Third, we used the global fitting method to directly fit the polynomial coefficients. We started by plotting the data sets corresponding to all ten currents, yielding a three-dimensional plot. The on-axis gradient was plotted as a function of current and z position. The combination of Eq. 2 and Eq. 4 was then fit to the three-dimensional data by varying the polynomial coefficients $p_0, ..., p_{37}$ and B_0. For this test, we returned to a constant effective length of $0.7m$ for all data sets. In this method, we avoided two different fitting processes by circumventing the fits for the Enge coefficients (c_{i_n} and c_{e_n}) and fitting the polynomial coefficients directly. We postulated this method to be the most accurate due to requiring only one fit and using a constant effective length.

Fourth, we performed the fit using the same global fit method described above, only changing the effective length determination method. Here, we determined the effective length for each data set numerically as in Eq. (3). Using these calculated effective lengths, we determined a formula for the effective length as a function of current by fitting the effective lengths for the ten data sets to a second degree polynomial as in Eq. (5).

$$L_{eff} = p_0 + p_1 I + p_2 I^2 \tag{5}$$

Eq. 4 and Eq. 5 were then substituted into Eq. (2) for the Enge coefficients and effective length respectively. The resultant function was then fit to the data from all ten data current sets, keeping the L_{eff} polynomial coefficients fixed. As before, we expected this method to be slightly less accurate than the method using a constant effective length. It does, however, result in a more reliable method for analysis of real SQ data.

In each fitting method, the final parameter values are heavily dependent on the initial values. Particularly, when there are many parameters to vary in the fitting process, the number of parameter sets which constitute satisfactory fits is large. Therefore, in the interest of obtaining consistent results

between all four fitting methods, a common set of initial values was set. For the local methods, the initial values of the coefficients were all set to constants. In the global methods, these initial values were set as the constant terms of their respective coefficient polynomials. The remaining polynomial coefficients were all initially set to zero.

5. TEST RESULTS: FITTING

Using each of the four fitting methods described, we fit an Enge function product to the simulated data for ten currents. The goal of the test was to observe the difference in the errors of the fitting processes as measured by the sum of the squared residuals. Of course, there is some systematic error in the fitting process. By setting the initial values of the global fit with constant effective length to the values used in the simulation, a minimum residual on the order of 10^{-9} was determined and attributed to systematic error. In each test, the total residual was recorded, and the results are shown in Table 1.

As expected, the global fitting methods proved to be more accurate, producing residuals roughly ten times as small as their local counterparts. An explanation for the higher accuracy of the global fits is twofold: they are limited to a single fitting procedure, and they presume the second-degree-polynomial behavior of the Enge coefficients with current. The local fits use two fitting procedures which naturally increases systematic error; and in the first fit, they do not assume that each c_{i_n} and c_{e_n} behaves as a second degree polynomial meaning each c_{i_n} and c_{e_n} is fit individually. That is, there is no inherent co-variance between the Enge coefficients and current when, according to the simulation, there is.

Shown in Fig. 1 are plots showing the results of each of the four fitting methods along with the expected behavior of the first three incident and exit coefficient polynomials. From the plots, we can see than none of the polynomials matches the expected polynomial behavior. This is likely due to the large number of parameters in the fit which allows for a plethora of possible parameter sets that minimize the squared residuals while not matching the parameters used in simulation. Note, however, that in simulating the data, the polynomial behavior for each c_{i_n} and c_{e_n} was set such that for all $n \in 0,...,5$ and $I \in \mathbb{R}$, $c_{i_n} = c_{e_n}$. We therefore expected the plots of c_{i_n} and c_{e_n} to match for each fit. We do indeed observe this behavior in Fig. 1.

Additionally, Fig. 1 exhibits a plot of the polynomial used to describe effective length as a function of current. This same polynomial was used in both the local and global fits employing a calculated effective length.

In Fig. 2, the difference in expected and fitted behavior produced by the global fit with constant effective length is displayed. The difference is measured as $\delta = \frac{b_{2,0_{fit}}}{b_{2,0_{exp}}} - 1$. We can see that in the majority of the fitted domain, the value of δ is approximately zero as we expect. However, nearing high z and I, δ increases. Likewise, in the current range approaching zero, the fitted function appears to undervalue the expected behavior. Given the final χ^2 value on the order of 10^{-2}, we can conclude that a majority of the error comes from the boundaries of the fit. Fitting all p_n coefficients provides

a completely general fit for any current or z position, allowing for ease of access to on-axis gradient data for an entire fixed radius.

To further test the range of the two global fitting techniques, we implemented a function to recursively fit the model in Eq. 2 to the on-axis gradient data (the local fits were not tested using this method due to the different number of initial and final parameters). Following each fit, the final parameters were recorded and subsequently used to create new initial parameters for the next minimization process. Shown in Fig. 3 are graphs of χ^2 plotted against the number of fit iterations. The minimum χ^2 value for each global fit is shown in Table 1. For both global fits, there was a initial decrease in the χ^2 value followed by a sharp drop and plateau. There were cases where the residuals increased, and in plotting, any increase in χ^2 was ignored and treated as a repeated value.

The relation between change in the residual squared and number of fits allows for an optimization of computing time. For the global fit with a calculated effective length, pursuing more than five fits will yield little increase in accuracy. In fitting globally with a fixed effective length, the number of useful fits increases to near ten, but results in a final decrease of only 1.2% of the initial χ^2. Final results for the maximum number of iterations are shown in table (1). Interesting to consider is the fact that after multiple fits, the χ^2 value for the calculated effective length drops below that for the constant effective length. Furthermore, there was a considerably larger percentage decrease applying the iterative algorithm to calculated effective length, also displayed in Table 1.

It is important to note that with respect to the time of each fitting process, there are increasing returns to scale. As the residuals decrease, the fitting procedure makes fewer calls and thus returns a final parameter set more quickly than in the previous fit. Therefore, although a higher number of iterations reaches a plateau in $\Delta\chi^2$, it is possible for the return to be great enough at a number of iterations past the plateau. We tested this possibility.

Shown in Fig. 3 are graphs of the decrease in residual, $\Delta\chi^2$, over the CPU time of operation plotted against the iteration number. In fact, we still see a sharp decrease and plateau of $\Delta\chi^2/CPU_{time}$. More specifically, in both the constant and calculated effective length fits, the decreases and the plateaus occur at the same points as the decreases in their corresponding plots of χ^2 versus iteration number. The correlation indicates increasing the number of iterations past the point where significant decreases in the squared sum of residuals occur is disadvantageous.

Fit Method	Local: L_{eff} fixed	Local: L_{eff} calc.	Global: L_{eff} fixed	Global L_{eff} calc.
χ^2 Single Fit	2.07×10^{-1}	1.30×10^{-1}	5.83×10^{-2}	5.97×10^{-2}
χ^2 Recursive Fit	——	——	5.76×10^{-2}	5.11×10^{-2}
% Decrease	——	——	1.71	14.4

Table 1. Residual sums squared for the four tested fitting methods. These are calculated as $\chi^2 = \sum(b_{fit} - b_{sim})^2$. The third row shows the resultant χ^2 values after the maximum number of minimizations as given by Fig. 3; thirty minimizations were used with L_{eff} calculated and L_{eff} constant. The final row displays the percentage decrease in the χ^2 value from the single fit to the recursive fit.
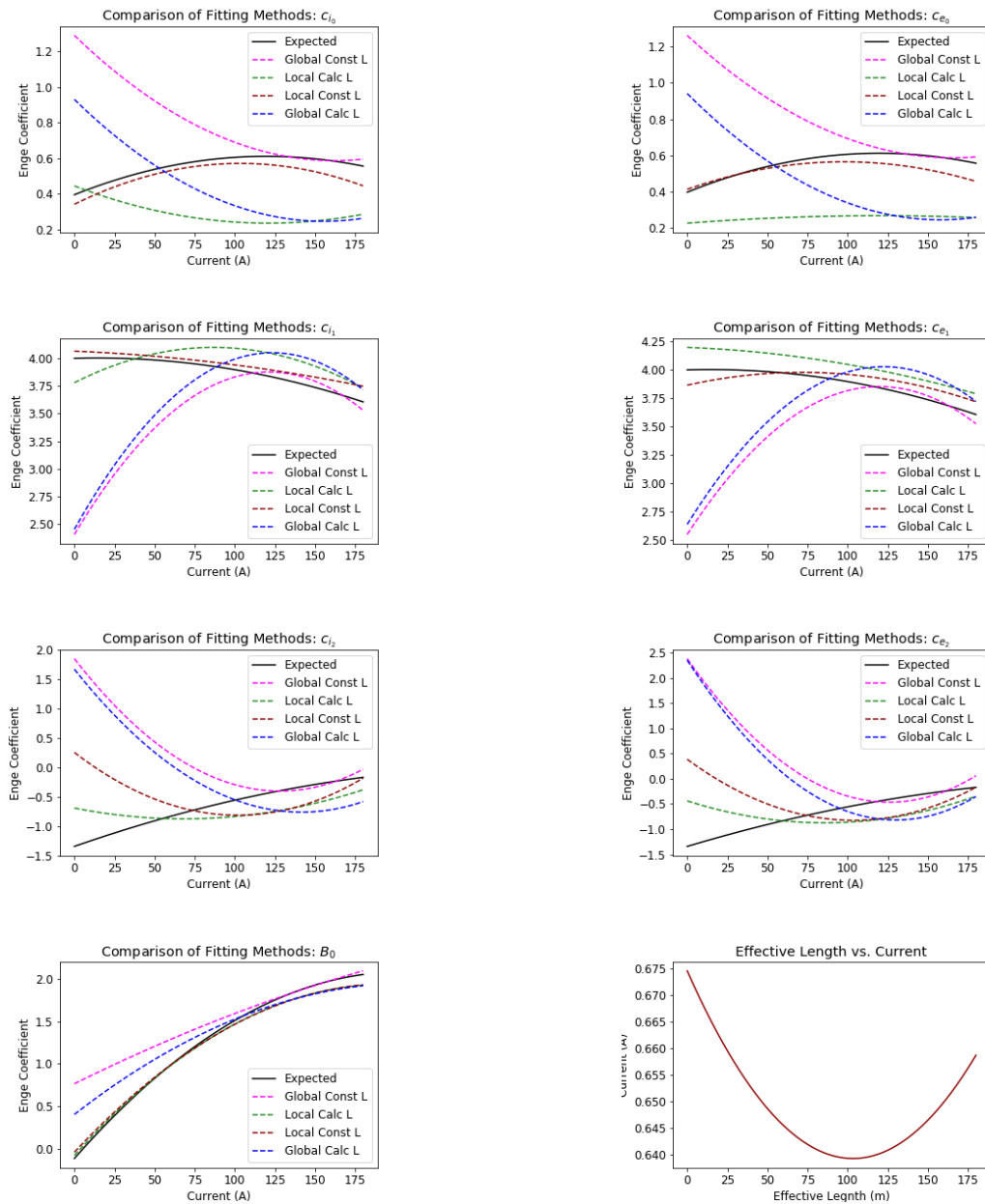
Figure 1. Expected versus fitted behavior for the first three incident and exit Enge coefficients, c_{i_n} and c_{e_n}, and the field gradient constant, B_0. Coefficients were fitted using all four fitting methods described above. While the local fit with constant effective length appears to yield a closer fit to the expected behavior, in fact the χ^2 for the global fit with constant effective length is on the order of ten times smaller than that for the local fits. Also shown is a plot of effective length versus current.
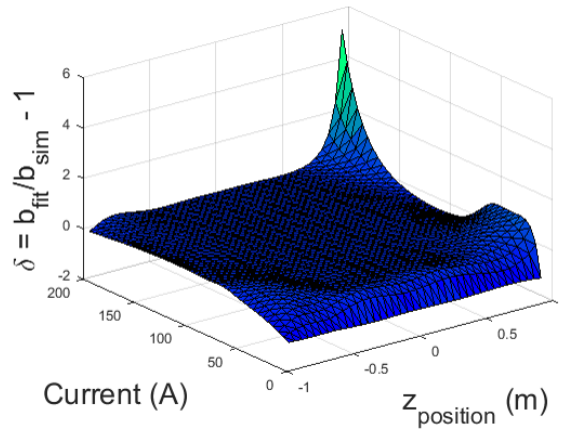
Figure 2. Difference in the fitted and expected behavior for the global fit with constant effective length. The difference is measured as $\delta = \frac{b_{2,0_{fit}}}{b_{2,0_{exp}}} - 1$. For a perfect fit, the result would be a plane at $\delta = 0$.

Figure 3. Plot showing χ^2 values and $\Delta\chi^2/CPU_{time}$ plotted against the number of fitting iterations for constant and calculated L_{eff} respectively.

6. CONCLUSIONS

Although the fixed effective length global fit yields the highest accuracy fit, it is not feasible to apply it in an experimental setting. The effective lengths of the SQs will not be known explicitly without calculation, and that variance must be accounted for in the fitting procedure. Therefore, we use this method to determine the maximum accuracy of the fit which is determined to be a minimum χ^2 on the order of 10^{-9}.

The optimal method to use in experiment is the global fit using a calculated effective length. Although the residual sum is higher than that for the constant effective length, it accounts for the natural behavior of the SQs and the unknown L_{eff}. Furthermore, under an iterative algorithm it has potential to make additional reductions in the χ^2 value.

We establish the optimal number of minimzations to perform to be approximately five based not only on the return on $\Delta\chi^2$ but also on the CPU performance time for each iteration of the fit. Increasing the iteration number beyond this yields little to no return in $\Delta\chi^2$.

In the future, we intend to test the fitting methods against data for operating SQs. Implementing the methods described here will decrease the time and cost of magnetic field mapping for SQs while simultaneously maximizing the accuracy. Moreover, the same procedure can be applied to superconducting or room temperature magnets of higher order poles with ease.

7. ACKNOWLEDGMENTS

References

[1] Takeda H., Kubo T., Kusaka K., Suzuki H., Inabe N., and Nolen J. A., 2013, "Extraction of 3D Field Maps of Magnetic Multipoles from 2D Surface Measurements with Applications to the Optics Calculations of the Large-Acceptance Superconducting Fragment Separator BigRIPS", Nuclear Instruments and Methods in Physics Research B 13, **798**

[2] Walstrom P. L., 2004, "Soft-Edged Magnet Models for Higher-Order Beam-Optics Map Codes", Nuclear Instruments and Methods in Physics Research A 519, **216**

Using Hadron resonance gas model to extract freezeout parameters at LHC energies

Tanmay Pani[**]

4th Year, Integrated Masters in Science,
National Institute of Science Education and Research,
Orissa, Jatani - 752050

Abstract. Hadron resonance gas (HRG) model gives a statistical description of hadrons in the grand canonical ensemble picture. It can be used to obtain the thermodynamic variables like Pressure, Entropy and Energy of the system. We have used one variant of the model called the excluded volume HRG in which the different hadrons are considered as hard spheres that follow the quantum statistics of bosons or fermions. We have used our HRG model to calculate the bulk thermodynamics of a gas of hadrons and compared those calculated from an ideal hadron gas (hadrons are considered as point particles) model and Lattice QCD data. Then we have used the number density of various hadrons calculated using the ideal HRG model, compared it to corresponding measured yields of hadrons in ALICE for Pb-Pb collisions at 2.76 TeV, to obtain the freeze-out volume and temperature.
Keywords: Hadron resonance gas (HRG) model, Freezeout parameters, LHC experiments.

1. THE HADRON RESONANCE GAS MODEL

The basic quantity required to compute the thermodynamical quantities is the partition function $Z(T, V)$ [1]. In the grand canonical (GC) ensemble, the partition function for a particle species i in the limit of large volume takes the following form ($k = \hbar = c = 1$):

$$\ln Z_i^{id.gas} = \frac{g_i V}{2\pi^2} \int_0^\infty \pm p^2 dp \ln(1 \pm \exp(-(E_i - \mu_i)/T)) \tag{1}$$

Where, g_i is the degeneracy factor, $E_i = \sqrt{p^2 + m_i^2}$ is the total energy of a particle with mass m_i and μ_i is the chemical potential of the ith species.

This integral can be solved analytically to obtain $\ln Z_i^{id.gas}$ as an infinite sum of bessel functions of second kind.

$$T \ln Z_i^{id.gas} = \frac{g_i m_i^2 V T^2}{2\pi^2} \sum_{n=1}^\infty \frac{(\pm 1)^{n-1}}{n^2} K_2\left(\frac{n m_i}{T}\right) \exp\left(\frac{n \mu_i}{T}\right) \tag{2}$$

[**] tanmay.pani@niser.ac.in

Pressure(P_i), number density(n_i), entropy density(s_i) and energy density(ϵ_i) obtained as:

$$n_i^{id.gas}(T, \mu_i) = \frac{T}{V} \left(\frac{\partial \ln Z_i^{id.gas}}{\partial \mu} \right)_{V,T} \tag{3}$$

$$P_i^{id.gas}(T, \mu_i) = \frac{T}{V} \ln Z_i^{id.gas} \tag{4}$$

$$\epsilon_i^{id.gas}(T, \mu_i) = -\frac{1}{V} \left(\frac{\partial \ln Z_i^{id.gas}}{\partial (1/T)} \right)_{\mu/T} \tag{5}$$

$$s_i^{id.gas}(T, \mu_i) = \frac{1}{V} \left(\frac{\partial \ln Z_i^{id.gas}}{\partial (T)} \right)_{V,\mu} \tag{6}$$

2. INTERACTING HADRON RESONANCE GAS MODEL

The preceding section describes hadrons that donot interact with each other. That is often not the case. Therefore, we also explore the cases where the hadrons interact. We start with adding a repulsive interaction by giving the hadrons dimensions (Excluded volume HRG).

2.1 *Excluded volume HRG*

For deriving the expressions for the thermodynamic variables in the excluded volume HRG, we need to solve the following transcedental equations[2][3]:

$$p^{ex}(T, \mu_1, \mu_2, \ldots, \mu_n) = p(T, \hat{\mu}_1, \hat{\mu}_2, \ldots, \hat{\mu}_n) \tag{7}$$

$$\hat{\mu}_i = \mu_i - v_{0i} p^{ex}(T, \mu_1, \mu_2, \ldots, \mu_n) \tag{8}$$

Where, $v_{0i} = (16\pi/3)R_i^3$, R_i being the radius of the ith hadron.

The other thermodynamic variables can be calculated as,

$$n_i^{ex} = \left(\frac{\partial p^{ex}}{\partial \mu_i} \right)_T = \frac{n_i(T, \hat{\mu}_i)}{1 + \sum_k v_{0k} n_k(T, \hat{\mu}_k)} \tag{9}$$

$$s_i^{ex} = \left(\frac{\partial p^{ex}}{\partial T} \right)_{\{\mu_i\}} = \frac{s_i(T, \hat{\mu}_i)}{1 + \sum_k v_{0k} n_k(T, \hat{\mu}_k)} \tag{10}$$

$$\epsilon_i^{ex} = Ts - P + \sum_k \mu_i n_i = \frac{\epsilon_i(T, \hat{\mu}_i)}{1 + \sum_k v_{0k} n_k(T, \hat{\mu}_k)} \tag{11}$$

One then can numerically calculate and compare the thermodynamic variables P,s and ϵ drawn from Ideal and Excluded volume HRG and lattice QCD calculations[4].
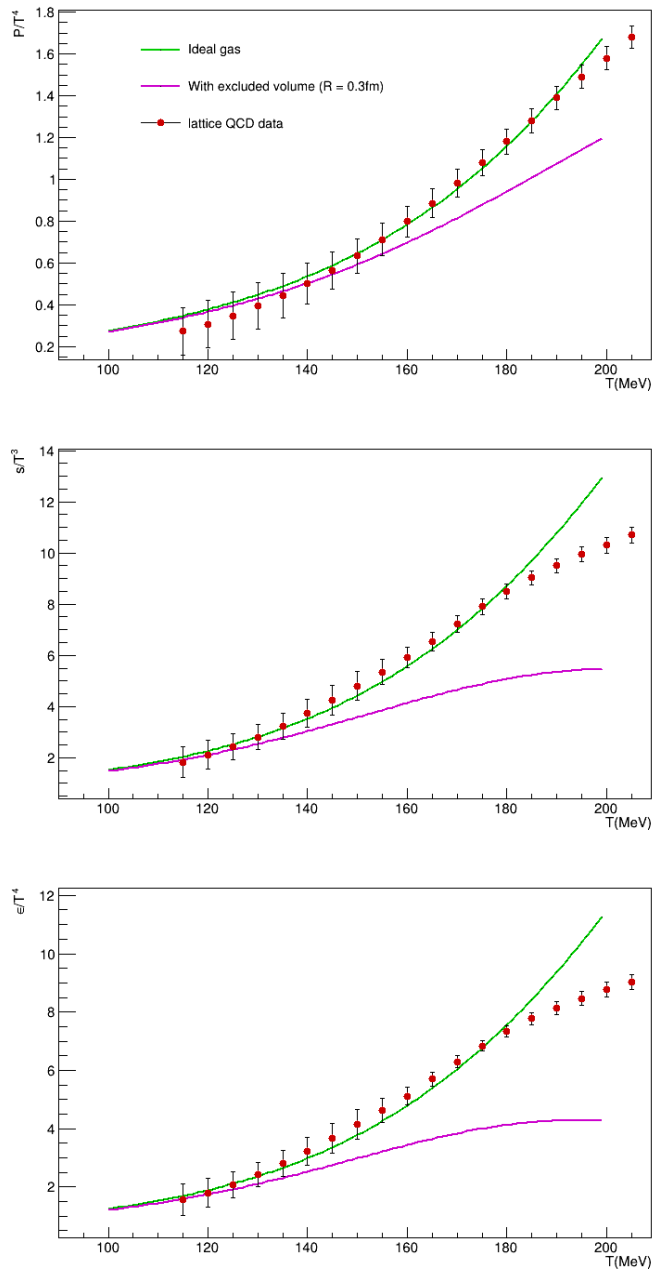
Figure 1. Pressure(top), Entropy density(middle) and Energy density(bottom) with ideal and excluded volume HRG, and comparision with lattice QCD[4].

From Fig. 1, it is apparent that the excluded volume consideration supresses the pressure,

entropy density and energy density compared to the ideal case. This supression becomes larger with temperature, as the mean distance between the hadrons keeps getting smaller compared to twice the radius considered in excluded volume HRG. Hadrons upto 2.25 GeV in mass have been considered, which includes 63 mesons and 59 baryons.

3. RESONANCE DECAY AND ESTIMATION OF YIELD

Until now, we were taking all the hadrons to be stable, and not considering their decays. But that is not the case. Most of the hadrons taken are unstable resonances that decay into lower mass hadrons. Considering resonance decay is imperative to estimating the yields of different particles at freezeout[5].

Therefore, we calculate the final multiplicity of a hadron species h as,

$$\langle N_h \rangle = V n_h + V \sum_R \langle n_h \rangle_R n_R \tag{12}$$

Where, V is the volume of the fireball, $V n_h$ is the primary yield of hadron h, n_R is the primary yield of resonance R and $\langle n_h \rangle_R$ is the average number of particles of species h from a decay of resonance R (also called the branching ratio). In this work, we have compared the yields obtained from the Ideal- HRG model, considering resonance decay to the yields, of $\pi^\pm$, $K^\pm$, K_0, p, $\bar{p}$, Λ, $\Xi^\pm$, $\Omega^\pm$ to corresponding measured yeilds in ALICE Pb-Pb collisions at $\sqrt{s_{NN}} = 2.76$TeV[6]. The branching ratios are obtained from the PDG[7].

As for LHC energies, the chemical potential tends to zero, we have set μ_B, μ_S and μ_Q to zero. The free parameters are the freezeout temperature (T) and volume (V). We have used the χ^2 minimization method to obtain T and V, where, χ^2 is defined as,

$$\frac{\chi^2}{N_{dof}} = \frac{1}{N_{dof}} \sum_{h=1}^{N} \frac{(\langle N_h^{exp} \rangle - \langle N_h \rangle)^2}{\sigma_h^2} \tag{13}$$

Where, $\langle N_h^{exp} \rangle$ and $\langle N_h \rangle$ are the experimental and theoretical hadron yields respectively, σ_h is the error in experimental yields and N_{dof} is the number of degrees of freedom calculated as the difference between the number of particles considered and the number of free parameters.

We calculated the χ^2 for a range of temperature and volume and then found the T and V for which the value of χ^2 is the lowest (shown in Fig.2).

For our considerations, we get a minimum χ^2/N_{dof} value of 8.08, at a Temperature of (163^{+9}_{-8})MeV and a fireball volume of $V = (3960^{+1240}_{-560})fm^3$.
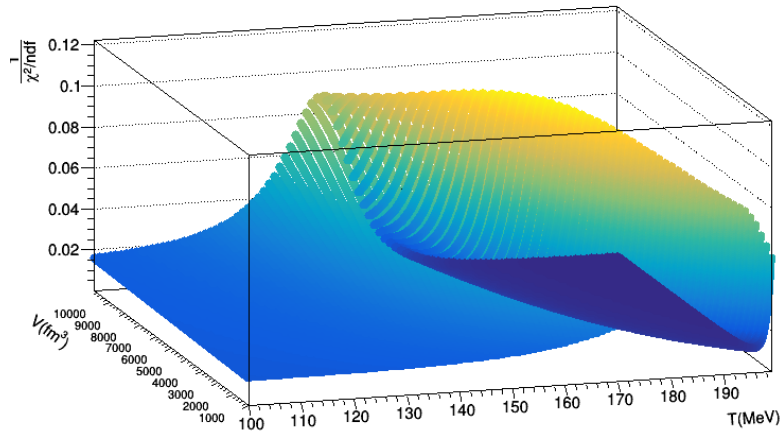
Figure 2. The plot of N_{dof}/χ^2 vs T and V

A comparision of the calculated and experimental yeilds have also been done in both graphically (Fig.3) and tabular manner (Table 1).

From table 1, we observe, that the light hadron yeilds are better determined than their heavier counterparts. This is because the limited number of resonance decays taken into account in our calculations. The heavier hadrons have more significant contributions from the heavy resonance decays than the lighter ones.
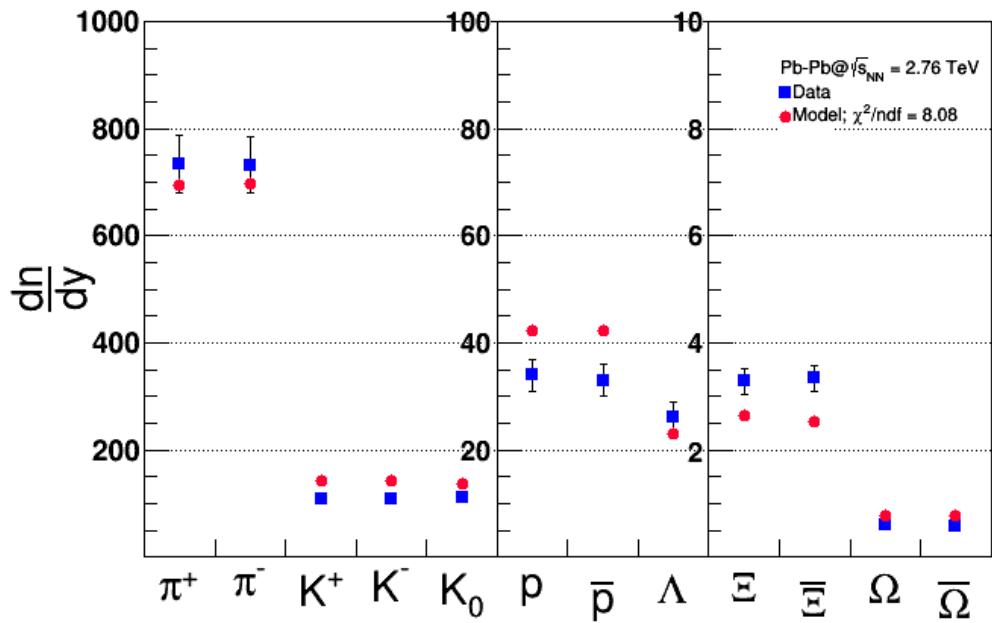
Figure 3. A comparison of experimental data[6] and model calculations for different particles.

Table 1. Experimental and Model Yields.

Particle	$\langle N_h^{exp} \rangle$	σ_h (Experimental error)	$\langle N_h \rangle$
π^+	733	54	693.46
π^-	732	52	695.88
K^+	109	9	143.06
K^-	109	9	143.097
K_0	110	10	138.055
p	34	3	42.17
$\bar{p}$	33	3	42.17
Λ	26	3	22.94
Ξ^+	3.28	0.247	2.64
Ξ^-	3.34	0.238	2.53
Ω^+	0.6	0.103	0.78
Ω^-	0.58	0.098	0.78

4. CONCLUSION

Through χ^2 minimization, we obtain the freezeout temperature and volume as (163^{+9}_{-8})MeV and $(3960^{+1240}_{-560})fm^3$ respectively for heavy-ion collisions at LHC energies.

5. ACKNOWLEDGEMENT

References

[1] R.Vogt, Ultra-relativistic heavy ion collisions, Elsevier (2007)

[2] A. Andronic et al. Phy. Lett. B 718(2012) 80-85

[3] D.H.Rischke, M.I. Gorenstein et al Z. Phys. C - Particles and Fields 51, 485-489 (1991)

[4] S. Borsanyi, et al., JHEP 1011 (2010) 077, arXiv:1007.2580.

[5] P. Alba, V. Vovchenko et al Nuc. Phy. A 974(2018) 22-34

[6] B. Abelev et al. [ALICE Collaboration], Phys. Rev. C 88, 044910 (2013).

[7] C. Patrignani et al. (Particle Data Group), Chin. Phys. C, 40, 100001 (2016) and 2017 update.

Study of Interface Layer and Fabrication of Perovskite Solar Cell (PSC)

Sandhya Negi[1], Md. Aatif[2], J. P. Tiwari[3], Sumita Srivastava[4]

Physics M.Sc. IIIrd Semester

[1,4] Department of physics, Pt. L.M.S. Government P.G. College, Rishikesh (Autonomous College)

[2,3]National Physical Laboratory, New Delhi, India

Sandhyanegi1997@gmail.com

Abstract: Perovskite solar cells (PSC) based on organometal halide light absorbers are considered as a promising photovoltaic technology due to their high power conversion efficiency (PCE) along with very low material cost. Since the first report on a long-term durable solid-state perovskite solar cell with a PCE of 9.7% in 2012, PCE as high as 19.3% was demonstrated in 2014, and a certified PCE of 17.9% was shown in 2014. In the present study, Perovskite Solar cells of the structure **ITO/PEDOT: PSS/CH$_3$NH$_3$PbI$_3$/LiF/Al** (Inverted structure) has been investigated. Fabrication of such cells involve cleaning the substrate, spin coating and deposition of the material on the substrate through thermal evaporation technique. After fabrication of solar cells, J-V characterization of these cells were carried out to determine the device parameters such as PCE, open circuit voltage (V_{oc}), fill factor (FF), and short circuit current density (J_{sc}). Future prospects of Perovskite Solar Cells are discussed.

Keywords: Perovskite Solar Cells (PSC), Organometal halides, Power Conversion Efficiency (PCE)

1. INTRODUCTION:

There is a current global need for clean and renewable energy sources. Fossil fuels are non-renewable and require finite resources, which are dwindling because of high cost and environmentally damaging retrieval techniques. So, there is an urgent need for cheap and sustainable resources. An efficient and more feasible alternative option is solar energy. Solar energy is more practical due to its plentiful availability; it is derived directly from the sun. Solar power is the key to a clean energy future.

PSC is a third generation solar cell. It consists of a perovskite compound, most commonly a hybrid organic-inorganic lead or tin halide based material, as the light-absorbing active layer. Perovskites possess intrinsic properties like broad absorption spectrum, fast charge separation, long transport distance of electrons and holes, long carrier separation life time that make them very promising materials for solid-state solar cells. Solar cell efficiencies of device using these materials have increased from 3.8% in 2009 to 22.1% in late 2017. PSCs are the fastest-advancing solar technology to date [1, 2, 3]. The structure of PSC is shown in Fig. 1. There are basically two types of PSC structures, one normal and the inverted. In the normal structure the electron transport layer (ETL) is sandwiched between the active perovskite layer and the Indium Tin Oxide (ITO) or Fluorine doped Tin Oxide (FTO) layer.
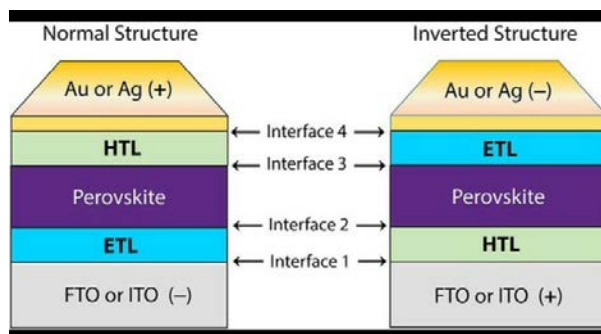
Fig. 1 Structure of Perovskite solar cell, ETL: electron transport layer. HTL: hole transport layer

where as the hole transport layer (HTL) is sandwiched between the perovskite layer and the metal (Au, Ag or Al) electrode. In the inverted structure the ETL and HTL layer positions are interchanged.

2. MATERIALS AND METHODS:

2.1 Materials

ITO: Indium Tin oxide (ITO) is colorless and transparent in thin layers, but it is yellow in bulk. ITO is a highly doped n-type semiconductor; it's band gap is around 4eV. In the present work ITO coated glass was used as one transparent electrode. It acted as the active layer to absorb light to generate free charge carriers. Its resistance was around 300-500 ohm/cm.

PEDOT:PSS (Hole Transport Layer-HTL): Poly (3,4-ethylenedioxythiophene) polystyrene sulfonate (PSS) is a polymer mixture of two ionomers. One component in this mixture is made up of sodium polystyrene sulfonate. Part of the sulfonyl groups are deprotonated and carry a negative charge. The other component PEDOT is a conjugated polymer and carries positive charges and is based on polythiophene. PEDOT:PSS is used as an antistatic agent to prevent electrostatic discharges during production and normal film use, independent of humidity conditions, and as electrolyte in polymer electrolytic capacitors.

PEDOT:PSS possesses many unique properties, such as good film forming ability by versatile fabricatipon techniques, superior transparency in visible light range, high electrical conductivity, intrinsically high work function and good physical and chemical stability in air. It has wide application in energy conversion and storage devices. PEDOT:PSS is being commonly used as the HTL.The mobility of hole in HTL is high.

The function of HTL is to transport the holes to the anode which are formed in active layer.When it is deposited above the ITO substrate, it avoid direct contact to the electrode with the perovskite layer and therefore increases the selectivity of the contact. This reduces the recombination of the holes and electrons(which are formed in the active layer) because it has high charge transporting properties as compared the active materials.

Methyl Ammonium Lead Iodide ($CH_3NH_3PbI_3$) (Active layer): $MAPbI_3$ plays an important role as a light absorber and long range hole diffusion length, at least 100 nm. It has either cubic or tetragonal lattice structure at room temperature. The bandgap of $MAPbI_3$ is 1.55eV. In the visible range the absorption coefficient of $MAPbI_3$ is around 1.0 x 10^5 (mol $L^{-1})^{-1}cm^{-1}$ at 550 nm. When the thickness of perovskite film ranges from 500-600 nm, it can absorb complete light in films (i.e no reflection of light will take place). At room temperature, $MAPbI_3$ crystallizes in a tetragonal unit cell. Above 327.4K, the unit cell undergoes a change in symmetry to become cubic, whereas below 162.2 K, the unit cell is orthorhombic. With a bandgap of 1.55 eV, this material is able to absorb incident light throughout the visible region and up to 800 nm. The valence and conduction band of $MAPbI_3$ are formed exclusively from Pb and I orbitals.

The methylammonium cation does not participate electronically in the band structure but governs the formation of the 3D perovskite crystal and therefore influences the optical properties of the material.

LiF (Electron Transport Layer-ETL): LiF has a good band alignment with adjacent layers and a good stability with the cathode interface. It stands out as a promising candidate due to its fabrication simplicity and stability. LiF is a wide band gap (>10 eV) material and is normally deposited via thermal evaporation. It is used as ETL to transport the electrons to the Cathode. It reduces the recombination of the free charge carrier with their counterparts which exist at the interface. It has high electron affinity and high electron mobility.

Aluminium: It is used as electrode. It is used to increase the work function of the ETL layer.

2.2 Experimental Procedure:

2.2.1 Active layer preparation

To synthesize the active layer CH_3NH_3 and PbI_2 were taken in desired concentration to prepare the perovskite absorber ($CH_3NH_3PbI_3$). Here 1:1 ratio of CH_3NH_3I and PbI_2 are used in DMF (Di methyl formamide) solution. The mixture was stirred for 12 hours with a magnetic bead at 70^0C.

2.2.2 Fabrication of Inverted PSC-Cleaning of the ITO substrates

Cleaning of the ITO substrate is an important step in the solar cell fabrication, because even a single particle or stain can disturb the uniformity of the film. Firstly the ITO coated substrate was washed with soap solution and DI (Deionized water) water. Then the substrate was sonicated for 15 minutes to remove the dust. In the next step, the substrate was rubbed by soap solution using cotton multiple times. After that sonication process was applied for 15 minutes. It was done to prevent ionic combination that may affect the proper operation of ITO. Then the substrate was boiled in acetone for 15-20 minutes in order to remove all the water droplets from the substrate. Finally, the samples were made to boil in Isopropanol for 20 minutes. It dissolved a wide range of non-polar compounds and acetone. It displaced water as well allowing surfaces to dry without spotting. Acetone leaves a residue, once dried is hard to remove, thus it was rinsed with isopropanol to remove the residue. Finally the substrate was put in vacuum oven at 100^0C for drying.

UV Ozone treatement

The UV-Ozone cleaning procedure is a highly effective method to remove a variety of contaminants from surfaces. This process has been carried out inside the glove box. A glovebox is a sealed container that is designed to allow one to manipulate objects when a separate atmosphere is desired

Coating of HTL layer and annealing

PEDOT:PSS was used as a hole transport layer. Coating of this HTL was done by a spin coater. The ITO substrate was kept inside the spin coater, held in high vacuum. The substrate was placed with ITO side facing up. Then the rpm was set for desired time. Spin coating is a procedure used to deposit uniform thin films on flat substrates. After that the substrates was annealed for 15 minutes at 140^0C for the evaporation of the solvent and to harden the deposited film into a semisolid form.

Coating of Active layer

Methyl ammonium lead iodide ($CH_3NH_3PbI_3$) was used as a active layer. The active layer was coated by spin coater at 1000 rpm for 30 sec and 3000 rpm for 30 sec for creating a uniform film. Thus the thickness of active layer was obtained was as 200nm. After this process, the substrate was annealed at 110^0C for 20-30 minutes.

Deposition of ETL layer

LiF was used as the ETL layer for PSC fabrication. Deposition of LiF layer was done using a thermal evaporator system. For this first a tungsten boat was flushed in which the material was to be loaded. The melting point of tungsten is 3422^0C. By resistive heating method the boat was flushed. Low vacuum of 3 X 10^{-2} Pa was created by a rotary vane pump and high vacuum of 5 X 10^{-6} Pa by a turbo pump. After that the LiF was deposited and then Al was deposited in the high vacuum atmosphere.

3. RESULT:

Current vs Voltage (J-V) curve of the inverted perovskite solar cell is shown in Fig. 2. Device parameters of fabricated perovskite solar cells are presented in Table 1.

Table 1: device parameters of fabricated perovskite solar cell

S.no	Device	Voc(V)	J_{SC}(mA/cm^2)	FF	Efficiency
1	ITO/PEDOT:PSS/MAPbI$_3$/LiF/Al	0.761	5.65X10^{-3}	0.202	0.8%
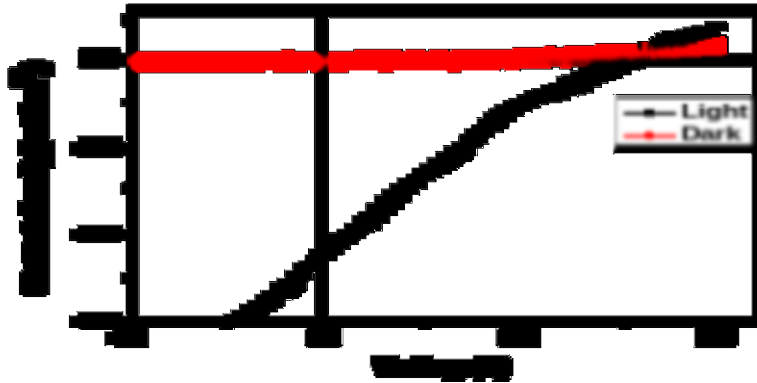
Fig.2 J-V Curve of the inverted perovskite solar cell

The efficieny of inverted device structure (ITO/PEDOT: PSS/$CH_3NH_3PbI_3$/LiF/Al) was expected to be 15%, but we got only 0.8%. The reasons of low stability are as follows-

- Degradation of perovskite material due to air
- Thickness and morphological issues in perovskite absorber and interfacial layer materials
- Ununiformity of Al electrode

CHALLENGE:- The long term stability of perovskite solar cells in a big issue. The degradation mechanism of perovskite materials is not clearly understood. An understanding of the degradation mechanism will be helpful to enhance the long-term stability, which will be a significant criterion for the commercialization of perovskite solar cells.

Water interacts strongly with commonly used perovskite material for solar cells,such as $MAPbI_3$. As the structure is soluble in water, the presence of humidity during film processing can significantly influence the thin film morphology.

4. CONCLUSIONS:

Fabrication of the perovskite solar cells using inverted device structure **ITO/PEDOT: PSS/CH₃NH₃PbI₃/LiF/Al** was demonstrated and the efficiency of .80% was achieved. The recent progress made in the device architectures and new materials open new opportunities for highly efficient and stable perovskite solar cells.

5. FUTURE PROSPECTS:

The development of perovskite solar cells in the last few years makes it a promising alternative for the next-generation, lowcost, and high-efficiency solar cell technology. Driven by the urgent need of cost-effective, high-efficient solar cells, PSCs have been intensively investigated in the recent years. Undoubtedly, halide perovskite materials have emerged as an attractive alternative to conventional silicon solar cells. It is suitable for flexible solar cell due to the low temperature processing and high efficiency.

PSC can be applied in photo-electrodes, radiation sensing and many more fields. The major problems in commercialization of PSC is the presence of toxic lead.

6. ACKNOWLEDGEMENTS:

References:

1. Hirasawa, M., Ishihara, T., Goto, T., Uchida, K. & Miura, N. Magnetoabsorption of the lowest exciton in perovskite-type compound (CH3NH3)PbI3. Physica B 201, 427–430 (1994).

2. Yuan, Y., Xiao, Z., Yang, B. & Huang, J. Arising applications of ferroelectric materials in photovoltaic devices. J. Mater. Chem. A 2, 6027–6041 (2014).

3. Frost, J. M. et al. Atomistic origins of high-performance in hybrid halide perovskite solar cells. Nano Lett. 14, 2584–2590 (2014).

A Study in Plasma Characteristics and Plasma–Ion Propulsion

Ninaad Desai

B.Sc. 3rd year / 5th semester, Department of Physics, St. Xavier's College (Autonomous), Gujarat University, Ahmedabad (ninaad98@gmail.com)

Abstract: In the present work, I have established and diagnosed some of the basic characteristics of plasma, such as relation between discharge voltage and pressure, plasma under external magnetic field and several related experiments which comprise the present work. Also, a simple and innovative model of an ion-propulsion engine has been developed for diagnostics and future demonstration purposes.

Keywords**:** Plasma, Electric discharge, Paschen's curve, Magneto plasma, Ion propulsion

1. INTRODUCTION

Plasma, being the fourth state of matter, provides the solution to many of our problems ranging from energy crisis to industrial applications and space exploration [1, 2, 3, 4]. An extensive research has been going on since many years in research labs in India and abroad as scientists have developed the potential applications of Plasma which range from plasma processing of materials to space explorations to even solving the future energy crisis by means of fusion.

2. PLASMA CHARACTERISTICS AND ION-PROPULSION

This project was carried out in collaboration with the Institute for Plasma Research, Gandhinagar where I was mentored by Mr. K.K. Mohandas. The main purpose of this project was to understand the physics of plasma and get a better appreciation of its applications in various industrial and scientific explorations.

2.1 Objectives

The following studies and objectives have been performed in the project:

1) To establish a relation between gas pressure and voltage in a discharge tube.

2) To observe the anomalies in gas pressure values after the electric discharge.

3) To observe and record the Paschen's curves plotted for gas discharge.

4) To map the magnetic field of the available magnets in the apparatus.

5) To measure the gas pressure and voltage values necessary for discharge under magnetic field.

6) To develop an ion-propulsion engine model worthy of providing experimental data as well as for future demonstrations.

The above-mentioned objectives have been performed under various conditions of the concerned parameters related to the experiments. So, the present article provides the outline of my work.

2.2 Figures for Plasma characteristics

Fig. 1 is the schematic diagram of the used set-up where AC signal is applied to the DIMMER-STAT.
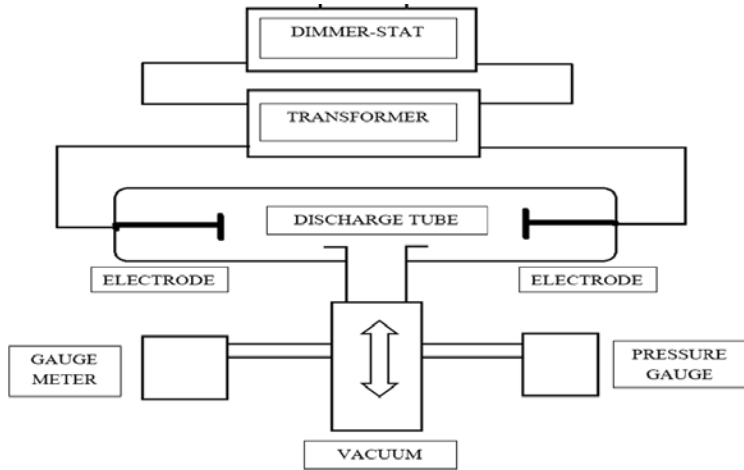
Figure 1. Block diagram of the apparatus set up.

The result of Objective-1 is shown in Fig. 2, which displays a piece-wise linear relation between Discharge voltage and Pressure corresponding to my data sets.
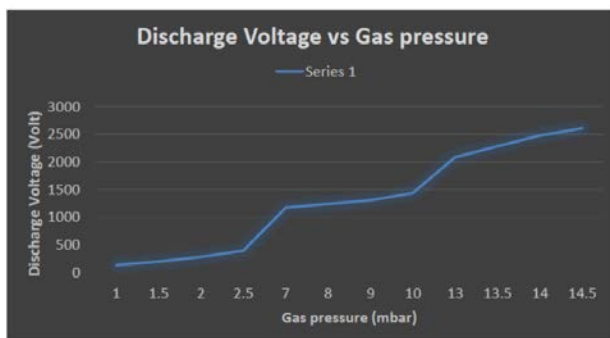

Figure 2. Relation between Discharge voltage and Pressure

The result of Objective-2 is shown in Fig. 3, which establishes that increase in voltage after discharge leads to a small increase in pressure values.
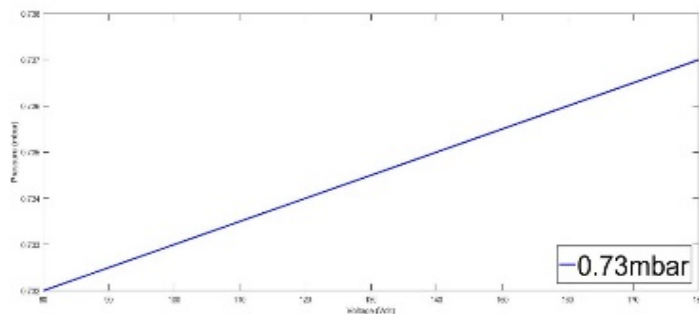
Figure 3. Anomalies in increase in Pressure after discharge
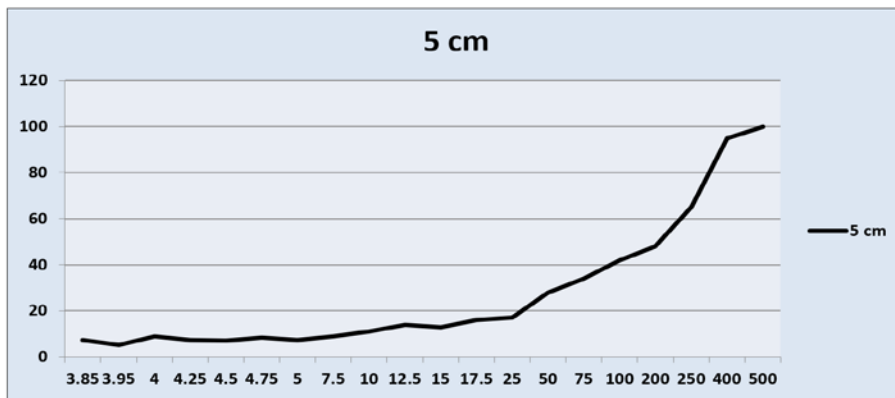
Y-axis: Volt / X-axis: atm*cm

Figure 4a. Experimental Paschen's Curve

Fig. 4a gives the Experimental Paschen's Curve. Fig. 4b is the ideal Paschen's Curve, where the highlighted segment of the same defines the range of the experimental parameters measured in the experiment.
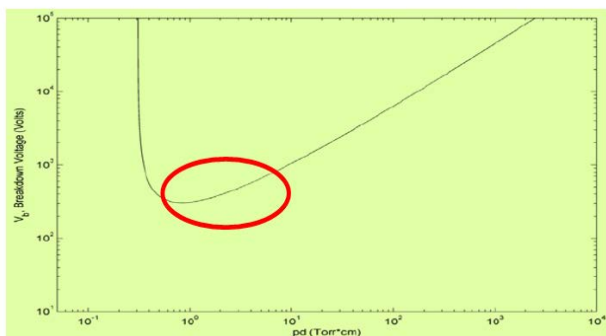

Figure 4b. Ideal Paschen's Curve

The results of the Objective-4 are represented in Fig. 5 which displays the effect of external magnetic field on the discharge voltage values. Here distance between the electrodes is 7 cm and letters 'a' and 'b' represent two distinct magnetic configurations.
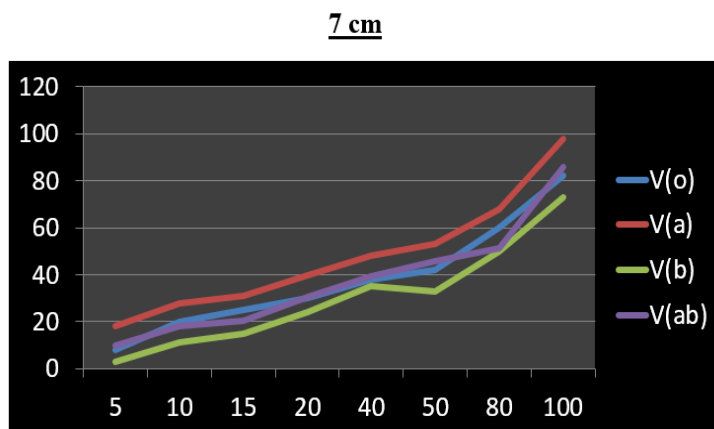
Y-axis: Discharge Volt / X-axis: atm

Figure 5. Discharge characteristics under external magnetic field

2.3 Ion-Propulsion

Ion thrusters are being designed for a wide variety of missions—from keeping communications satellites in the proper position to propelling spacecraft throughout our solar system. These thrusters have high specific impulses—ratio of thrust to the rate of propellant consumption, so they require significantly less propellant for a given mission than would be needed with chemical propulsion. Ion propulsion is even considered to be mission enabling for some cases where sufficient chemical propellant cannot be carried on the spacecraft to accomplish the desired mission.

An innovative and experimental model of an ion-propulsion engine has been developed for simple diagnostics and demonstration purposes which is shown in Fig. 6.

The model is consisting an electrode in the form of a nail which ionizes the atoms surrounding its tip through the phenomenon of Corona discharge, when it is biased. The ions created are thus accelerated towards the hollow cylinder, which functions as the cathode. After passing through the hollow cylinder, the ions hit the graphite slab which works as a Faraday's cup and it is connected to an output circuit to display the result on the screen of the oscilloscope.
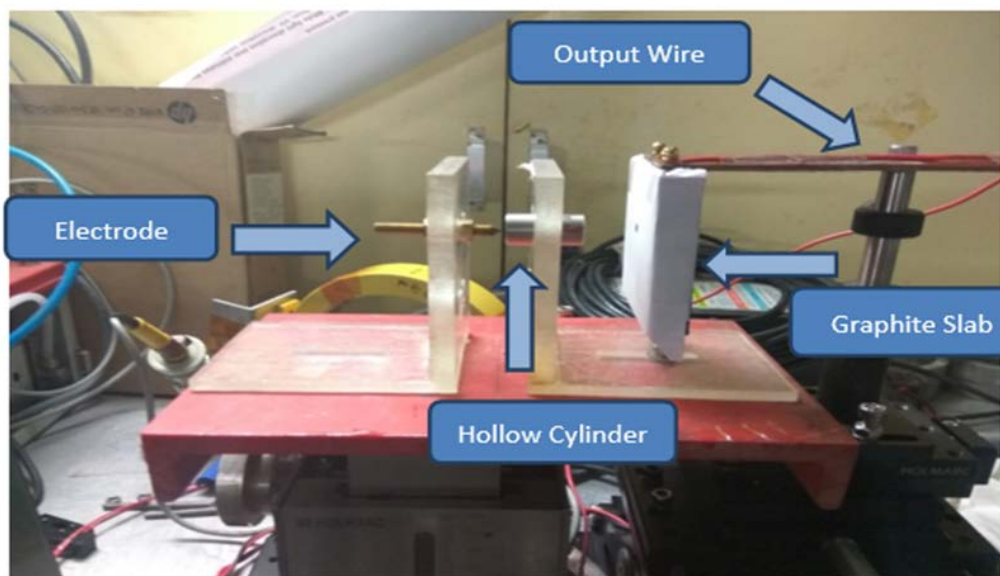

Figure 6. Ion-Propulsion engine model

2.4 Future study

1) Future studies involving discharge voltages and pressure could be done by varying the distance between the electrodes. Also, certain basic changes in the experimental system which allows measurement of plasma density and temperature using different diagnostic systems. Magnetic mirror confinement and its diagnostics are also possible.

2) Further scope in ion propulsion includes trying out various combinations of magnetic configurations, permanent or electromagnetic, to efficiently channelize the ion beam and to vary the distance of the graphite slab as well as to alter the open area of the slab to optimize the output of ions in terms of distance and thrust.

3. ACKNOWLEDGEMENT

References

[1] F. F. Chen, Introduction to Plasma Physics and Controlled Fusion, vol. 1: Plasma Physics. Plenum Press, 1984.

[2] Michel A. Lieberman, Principles of Plasma Discharges and Material Processing, Second Edition, Wiley Publications, 2005.

[3] The physics of plasmas by Richard Fitzpatrick in association with R.D. Hazeltine and F.L. Waelbroeck (PDF version).

[4] Fundamentals of Plasma Physics by J.A. Bittencourt (PDF version).

STUDENT JOURNAL OF PHYSICS

CONTENTS

ARTICLES